



The Spatial and Temporal Variations of Turbulence in a Solar Flare

Morgan Stores¹ , Natasha L. S. Jeffrey¹ , and Eduard P. Kontar² ¹ Department of Mathematics, Physics & Electrical Engineering, Northumbria University, Newcastle upon Tyne NE1 8ST, UK² School of Physics & Astronomy, University of Glasgow, Glasgow G12 8QQ, UK

Received 2021 July 5; revised 2021 October 1; accepted 2021 October 1; published 2021 December 9

Abstract

Magnetohydrodynamic plasma turbulence is believed to play a vital role in the production of energetic electrons during solar flares, and the nonthermal broadening of spectral lines is a key sign of this turbulence. Here, we determine how flare turbulence evolves in time and space using spectral profiles of Fe XXIV, Fe XXIII, and Fe XVI, observed by the Hinode/EUV Imaging Spectrometer. Maps of nonthermal velocity are created for times covering the X-ray rise, peak, and decay. For the first time, the creation of kinetic energy density maps reveal where energy is available for energization, suggesting that similar levels of energy may be available to heat and/or accelerate electrons in large regions of the flare. We find that turbulence is distributed throughout the entire flare, often greatest in the coronal loop tops, and decaying at different rates at different locations. For hotter ions (Fe XXIV and Fe XXIII), the nonthermal velocity decreases as the flare evolves and during/after the X-ray peak shows a clear spatial variation decreasing linearly from the loop apex toward the ribbon. For the cooler ion (Fe XVI), the nonthermal velocity remains relatively constant throughout the flare, but steeply increases in one region corresponding to the southern ribbon, peaking just prior to the peak in hard X-rays before declining. The results suggest turbulence has a more complex temporal and spatial structure than previously assumed, while newly introduced turbulent kinetic energy maps show the availability of the energy and identify important spatial inhomogeneities in the macroscopic plasma motions leading to turbulence.

Unified Astronomy Thesaurus concepts: Solar flares (1496); Solar energetic particles (1491); Solar corona (1483)

1. Introduction

During a solar flare, energy stored in twisted and stressed coronal magnetic fields is rapidly released by magnetic reconnection (e.g., Parker 1957; Sweet 1958; Priest & Forbes 2000), resulting in low-lying flare loops. The magnetic energy released by reconnection is partitioned into thermal and nonthermal particle energies (e.g., Emslie et al. 2012; Warmuth & Mann 2016; Aschwanden et al. 2017), as well as kinetic energy in the form of plasma motions and turbulence in the coronal loop tops of flares (Melrose 1994; Kontar et al. 2017).

Magnetohydrodynamic (MHD) plasma turbulence (stochastic motions of the magnetized plasma), a product of reconnection, can drastically affect the dynamics of the reconnection process itself and transfer energy facilitating particle energization and heating over 10 MK (e.g., Larosa & Moore 1993; Petrosian 2012; Kontar et al. 2017) via the cascade of energy to smaller and smaller scales (Klein & Dalla 2017) and eventually dissipation at the particle level (e.g., Miller et al. 1997; Krucker et al. 2008; Petrosian 2012). This rate of particle energization is determined by both the rate of energy release at large scales and the rate of energy transfer to smaller scales. Within these regions of turbulence, charged particles can also become trapped by turbulent scattering off magnetic fluctuations, particularly high-energy MeV electrons (Musset et al. 2018). Thus, the presence of turbulence in flares is intimately linked with both electron acceleration and transport. The properties of the solar flare plasma can be determined from observing and analyzing the properties of optically thin spectral lines in the solar atmosphere (e.g., see the reviews by Milligan 2015;

Del Zanna & Mason 2018) with instruments such as the Hinode (Kosugi et al. 2007) EUV Imaging Spectrometer (EIS; Culhane et al. 2007) providing spatially resolved information on ion line emissions, plasma temperatures, mass flows, ion abundances, and electron densities. Spectral line width or broadening is produced by many small shifts in wavelength caused by both microscopic ion motions and macroscopic plasma motions of the emitting ion. During a flare, spectral lines often show line widths in excess of what is expected from random thermal motions alone (thermal broadening or velocity). The excess broadening (nonthermal broadening or velocity) is believed to be the result of superposed Doppler-shifted emission of (1) turbulent fluid motions and/or (2) the superposition of flows from different loops. Recently Polito et al. (2019), using hydrodynamic simulations of multi-thread flare loops with the 1D RADYN code (Carlsson & Stein 1992; Allred et al. 2015), suggested that nonthermal broadening cannot be easily reproduced by such flows, with turbulent motions most likely to be the cause. Alternative mechanisms may cause line broadening, such as opacity or pressure broadening. However as the solar flare plasma is optically thin (e.g., Levens 2018), these should be negligible (e.g., Milligan 2011). Spectral line broadening is usually extracted by fitting a Gaussian profile to the line, as such a line shape is expected from a thermal ion velocity distribution and indeed from any plasma motions undergoing Brownian motion. However, it has also been suggested that the line shape may provide a diagnostic of the underlying turbulent plasma motions (e.g., Jeffrey et al. 2016, 2017; Polito et al. 2018) where non-Brownian plasma motions or the spectrum of plasma/magnetic fluctuations have a non-Gaussian or Lorentzian form (e.g., Kontar et al. 2014); then different spectral line shapes should indeed be expected.

Nonthermal broadening has been extensively studied in solar flares and hence serves as a key signature of turbulence. Early



Original content from this work may be used under the terms of the [Creative Commons Attribution 4.0 licence](https://creativecommons.org/licenses/by/4.0/). Any further distribution of this work must maintain attribution to the author(s) and the title of the work, journal citation and DOI.

studies using soft X-rays (SXR) were spatially unresolved (e.g., Doschek et al. 1980; Antonucci et al. 1982; Antonucci & Dodero 1995), but they showed: (1) nonthermal motions preceding the convective motions caused by chromospheric evaporation, suggesting that nonthermal broadening is due to the primary energy release, and (2) a strong temperature dependence where regions of high temperature and hence lines formed at the highest temperatures show the greatest nonthermal broadening. More recently, spatial changes in nonthermal broadening have also been examined (e.g., Doschek et al. 2014; Warren et al. 2018) using Hinode/EIS and also with the Interface Region Imaging Spectrograph (IRIS; De Pontieu et al. 2014). Spatially resolved observations often show that nonthermal broadening increases with both temperature and height in the coronal loop source. Interestingly, although turbulence is often discussed as a product of reconnection in the corona, the presence of nonthermal broadening during the flare is not a phenomenon only localized high in the coronal loops. For example, Milligan (2011) looked at both bulk Doppler flows and nonthermal broadening in cooler lines formed in the low corona close to flare X-ray footpoints. Jeffrey et al. (2018) studied Si IV formed in the lower transition region during a flare. The high time cadence observations using IRIS showed that nonthermal broadening increased a full 10 s before heating in the region, strongly suggesting turbulence played a role in the heating. Moreover, the temporal evolution of both bulk velocity and nonthermal velocity could be reproduced by plasma fluctuations caused by the interaction of different waveforms in the region.

In this study, we perform a thorough investigation of the spatial and temporal distribution of nonthermal spectral line broadening (turbulence) in one flare. We map how the nonthermal broadening and kinetic energy of plasma motions change throughout the entire flare in order to determine how the distribution and magnitude of turbulence changes with temperature, time, and space. The nonthermal broadening and turbulent kinetic energy from various ions is mapped using EUV spectral lines from Hinode/EIS formed between ≈ 6.3 and 15.8 MK. High-resolution EUV spatial images from the Atmospheric Imaging Assembly (AIA; Lemen et al. 2012) aboard the Solar Dynamic Observatory (SDO) are used in conjunction with EIS data to map the nonthermal broadening to flare features, such as the coronal loop top source and the ribbon features, and to different loops produced as reconnection progresses. An overview of the data is provided in Section 2. Section 3 presents the results and the findings of the study are summarized in Section 4.

2. Observational Overview

This paper studies the X1.2 solar flare, SOL2013-05-15T01:45 shown in Figure 1. The Geostationary Operational Environmental Satellite (Kahler & Kreplin 1991) light curves in Figure 1 show the SXR emission, corresponding to the heated plasma, peaking at approximately 01:45 UT. Light curves from the (Reuven) Ramaty High Energy Solar Spectroscopic Imager (RHESSI; Lin et al. 2002), see Figure 1, show the hard X-ray (HXR) emission, usually corresponding to accelerated electrons, rising and peaking at approximately 01:34:00 UT and 01:42:00 UT respectively. To study different flare features, AIA images at several wavelengths were examined, including 131 Å and 304 Å. Figure 1 shows an AIA 131 Å image of the flare at 01:30:34 UT, with 131 Å contours (black) at levels of 50%, 70%, and 90% of the maximum 131 Å image value, and 304 Å contours (pink) at levels of 40% and 80%, of the maximum 304 Å image value

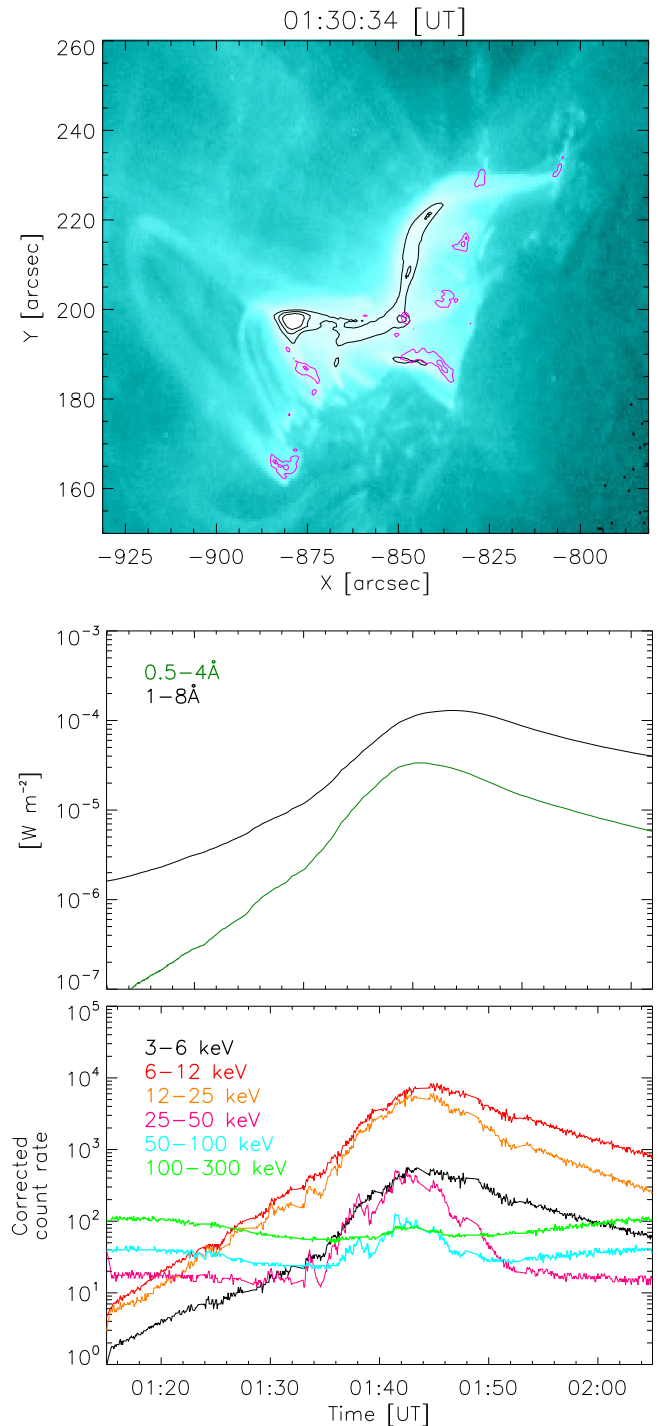


Figure 1. Atmospheric Imaging Assembly (AIA) 131 Å image (top) taken at 01:30:34 UT of the X1.2 flare SOL2013-05-15T01:45. Black contours show AIA channel 131 Å intensity levels at 50%, 70%, and 90% of the maximum 131 Å image value (units of $\text{DN s}^{-1} \text{px}^{-1}$). Pink contours show AIA channel 304 Å intensity levels at 40% and 80% of the maximum 304 Å image value. Geostationary Operational Environmental Satellite and Ramaty High Energy Solar Spectroscopic Imager (RHESSI) soft and hard X-ray (middle and bottom) flare light curves, respectively, are shown, peaking at approximately 01:45:00 UT and 01:42:00 UT, respectively. These observations coincide with the time of EUV Imaging Spectrometer observations that range from 01:25:14 UT to 01:51:58 UT.

(units of $\text{DN s}^{-1} \text{px}^{-1}$). Cooler channels such as 304 Å highlight the ribbon features of the flare, while the hotter channels such as 131 Å highlight the coronal source and hot flaring loops.

Table 1
Hinode/EIS Spectral Lines Studied

Ion	Wavelength (Å)	Temperature $\log_{10} T$ (K)	Thermal velocity (km s ⁻¹)
Fe XXIV	192.0285	7.2	70.0
Fe XXIV	255.1136	7.2	70.0
Fe XVI	262.9760	6.8	44.1
Fe XXIII	263.7657	7.2	70.0

2.1. Hinode/EIS Spectral Data

Prior to this solar flare, there were multiple large flares in the active region. This study utilizes Hinode/EIS spectral line data between the times of 01:30:34 UT and 01:51:58 UT, covering the rise, the peak, and part of the decay phase of the flare, as shown in Figure 1. During this time EIS operated using the 2'' slit in fast rastering mode. This results in a reduced spatial resolution in the x direction, $\sim 5.99''$ and a temporal resolution of approximately 9 s. The EIS field of view observing the flare region is $(30 \times 5.99'') \sim 179'' \times 152''$.

During the studied time frame, five EIS observations are available and each set of data contains 10 spectral windows. Here, the stated time of an observation is at the beginning of the raster time. SolarSoftWare (SSW) routine `eis_prep.pro` converted the raw EIS data to level 1 data. This routine removes saturated data, detector artifacts, cosmic ray hits, and missing data packets. In order to study the line profiles, strong spectral lines are required that have no blending with other lines. The spectral lines investigated are given in Table 1 where the data were obtained from the CHIANTI database (Dere et al. 1997, 2019). These lines were initially chosen for their high intensity and high formation temperatures, forming in different regions of the flaring corona.

Due to the high cadence of AIA data, there are image data available that correlate to the time of the EIS data observations within 10 seconds. To align EIS with the AIA images, EIS Fe XXIV (192.0285 Å) images were aligned to AIA 193 Å.³ The routine `eis_aia_offsets.pro` was also used to check the alignment between the two data types. This routine has an uncertainty of $\sim 5''$ which compared to the EIS field of view is small. Thus, the maximum alignment uncertainty is $\sim 5''$.

2.2. EIS Spectral Line Fitting and Analysis

This study only examines optically thin spectral lines. Thus, properties such as line shape and broadening can be related to the underlying ion velocity distribution that is assumed to be an isothermal Maxwellian ion distribution.⁴ Hence, all studied lines with intensity $I(\lambda)$ are fitted with the following Gaussian function:

$$I(\lambda) = I_B + I_0 \exp\left(-\frac{(\lambda - \lambda_0)^2}{2\Delta\lambda^2}\right), \quad (1)$$

where λ is the wavelength (Å), I_B is the background intensity ($\text{erg cm}^{-2} \text{s}^{-1} \text{sr}^{-1} \text{Å}^{-1}$), I_0 is the peak intensity

³ Fe XXIV (192.0285 Å) accounts for around 80% of the total intensity of AIA 193 Å (Kontar et al. 2017).

⁴ The study of Jeffrey et al. (2016) determined non-Gaussian line shapes in certain regions of this flare, but the isothermal Maxwellian assumption is appropriate for the study outlined here.

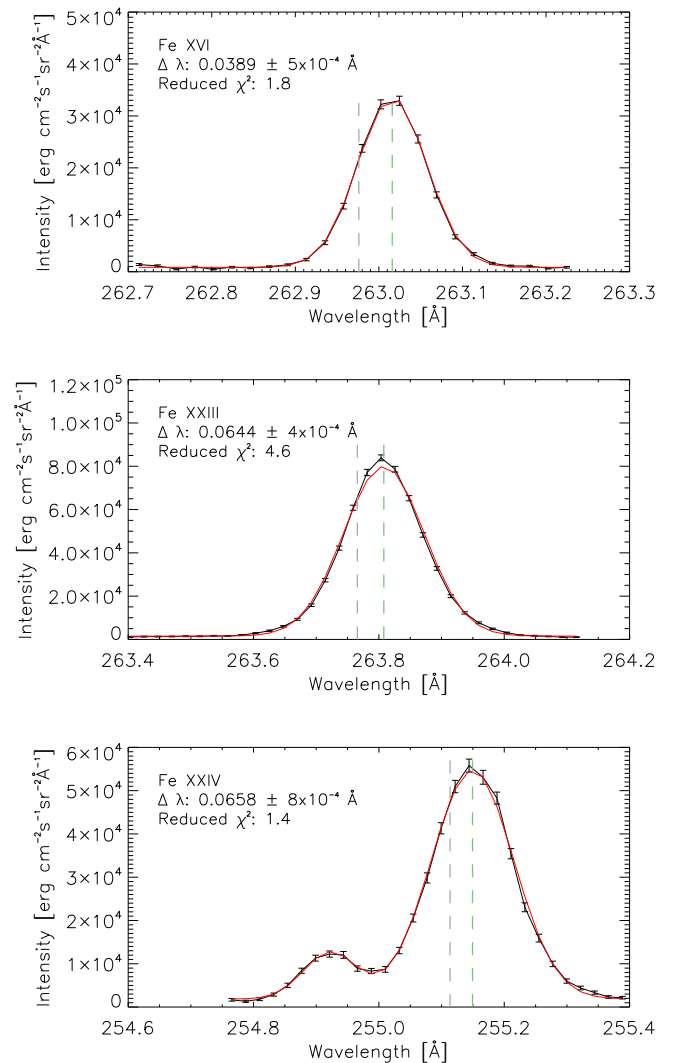


Figure 2. Example Gaussian fits for spectral lines included in the study. Top to bottom: lines and fits for Fe XVI, Fe XXIII, and Fe XXIV respectively. The red line shows the Gaussian fit while black points show the data. The rest (laboratory) wavelength of the ion is indicated by the gray dashed line in each panel while the observed centroid is shown by the green dashed line and shifted by 0.0400 Å, 0.0422 Å and 0.0357 Å for Fe XVI, Fe XXIII, and Fe XXIV respectively. The values of the total line broadening \pm uncertainty ($\Delta\lambda$ [Å]) and reduced χ^2 value are stated in the legend of each panel. Some Fe XXIV lines required a double Gaussian fit to remove blends (bottom panel).

($\text{erg cm}^{-2} \text{s}^{-1} \text{sr}^{-1} \text{Å}^{-1}$), λ_0 is the measured centroid position (Å), and $\Delta\lambda$ is the line broadening (Å).

As shown in Figure 2, many of the line centroid positions are redshifted compared to their laboratory rest position, by ~ 0.04 Å. This indicates the presence of bulk motions in the plasma moving away from the observer. In Jeffrey et al. (2017), a similar observation in a close to disk center flare (SOL2014-03-29T17:44) suggested the presence of plasma down-flows alongside spectral line broadening and line shape changes. Indeed, turbulent flows are expected in the flaring corona, due to high Reynolds numbers (e.g., Priest 2014).

The spectral lines discussed here are formed over different temperatures: the coolest ion studied is Fe XVI (262.9760 Å) which according to CHIANTI forms at ~ 6.3 MK, but the contribution function for Fe XVI peaks at ~ 2 –4 MK (e.g., Jeffrey et al. 2016); Fe XXIII (263.7657 Å) which forms at

~ 15.8 MK; and Fe XXIV (192.0285 Å and 255.1136 Å) also forming at ~ 15.8 MK but with a larger contribution function at $\log_{10} T > 7.2$ compared to Fe XXIII (e.g., Graham et al. 2013).

Analysis of the EIS spectral lines and corresponding Gaussian fits ensured only suitable lines remained in the study. Spectral lines were considered unsuitable and removed from the study if they were very saturated, noisy (defined as the ratio of the intensity uncertainty to intensity), did not have an accurate Gaussian fit, or contained other line components.

Often, a small line component lying in the blue wing of Fe XXIII is observed. There is no documented line at this location in the CHIANTI database and the line could be due to bulk motions along the line of sight. Fe XXIII lines containing the shifted component were removed from the study. Similar components were also seen in the blue wing of Fe XVI (262.9760 Å); these lines were also removed from the study.

Fe XXIV was originally observed at 192.0285 Å. Due to high saturation at this wavelength during the flare, this line was discarded. Instead, the Fe XXIV line found at 255.1163 Å was studied. The spectral line Fe XVII (254.8853 Å) sits in the blue wing of Fe XXIV (255.1136 Å). Due to the spectral resolution of the instrument, 47 mÅ full width half maximum (FWHM) at 185 Å, EIS is not always able to resolve blended spectral lines. However, it is possible to separate the emission from each blended component by fitting multiple Gaussian components. A simple two-Gaussian fit is successful in eliminating the influence of Fe XVII in the wing.

The spectral lines studied have a high intensity during the flare. Thus, noise was reduced by applying a lower intensity limit, ensuring that the pixels studied were related to the flare, not background activity. To further reduce the amount of noise, pixels were binned in the y -direction.

In order to see how the binning size affected the line broadening, pixels were binned in grouping sizes 2''–5''. Comparing the different binning sizes, we determined no significant change in line broadening with changing binning size. Thus, a binning size of 4'' was found to be suitable; the resulting spectral lines were of high intensity but contained enough spatial information to compare with the flare features.

To determine the accuracy of the Gaussian forward fitting to the spectral line data, the goodness of fit was measured using a standard reduced chi-squared statistic χ^2 . Reduced χ^2 maps were created for each ion at each observation time and any Gaussian fits with a reduced χ^2 value greater than 5 were extracted and examined carefully by eye. If the spectral line or Gaussian fit was deemed unsuitable the pixel was removed from the study.

3. Results

3.1. Maps of Nonthermal Broadening

To determine the nonthermal broadening from the total line broadening $\Delta\lambda$, first, the FWHM (Å) of each spectral line was calculated using

$$\text{FWHM} = 2\sqrt{2\ln 2} \Delta\lambda. \quad (2)$$

A nonthermal velocity v_{nth} (km s^{-1}), associated with the turbulent plasma motions, can be extracted from the line broadening by rearranging the following equation (e.g., Brooks & Warren 2016), which relates the FWHM with the individual

thermal, nonthermal, and instrumental broadening components:

$$\text{FWHM} = \sqrt{4\ln 2 \left(\frac{\lambda_0}{c}\right)^2 \left(\frac{2k_B T_i}{m} + v_{\text{nth}}^2\right) + \text{FWHM}_I^2}, \quad (3)$$

where the thermal velocity is given by $\sqrt{2k_B T_i/m}$ (Table 1), and c is the speed of light, k_B is the Boltzmann constant, T_i is the ion temperature (K) and m is the mass of the ion (g). FWHM_I is the instrumental FWHM (Å) that was determined using SSW routine `eis_slit_width.pro`.

Maps of nonthermal velocity, together with AIA 94 Å images (top row), are shown in Figure 3, for each ion studied at each observed time, from 01:30:34 UT to 01:51:58 UT. Rows 2–4 show a different ion, increasing in temperature. From top to bottom this corresponds to Fe XVI, Fe XXIII, and Fe XXIV. Each column shows a different observation time, with the time increasing from left to right. The AIA 94 Å⁵ contours (extracted intensity levels that range between 25% and 80% of the maximum 94 Å image value) overlaid onto the nonthermal velocity maps clearly denote the flare cusp and hot loops/loop tops (blue) while cooler material such as the flare ribbons are shown by AIA 304 Å contours (white) at levels ranging from 20% to 90% of the maximum AIA 304 Å image value.

The nonthermal velocity maps of Fe XXIII and Fe XXIV follow similar trends. First, we observe the presence of relatively high nonthermal velocities throughout the flare structures with values ranging between $v_{\text{nth}} = 113.24 \pm 2.40$ km s^{-1} and $v_{\text{nth}} = 22.70 \pm 1.30$ km s^{-1} early in the flare, before the peak in HXRs. At these early times, there is no strong pattern in space associated with the nonthermal velocity (or turbulence) and the v_{nth} values in these maps appear more random or “chaotic” compared to later times. However, as the flare progresses to times during and after the HXR peak (01:41:16 UT to 01:51:58 UT), clear spatial patterns appear, with the largest values of nonthermal velocity present at the coronal loop top/cusp and decreasing toward the ribbon features/smaller radial distances in the map. By the last observation, at 01:51:58 UT, the region of largest nonthermal velocity is in the upper left quadrant of the maps (approximately $-900'' \leq x \leq -870''$ and $200'' \leq y \leq 215''$). Much of this region does not overlap with the AIA 94 Å contours in this map; these regions of high nonthermal velocity now sit at greater radial distances compared to the highest 94 Å intensity values in the lower loops. At this time, the cooler Fe XVI maps show nonzero nonthermal velocity values closer to the lower loop region shown by the 94 Å contours, suggesting that the cooling plasma in these loops may still suffer from some turbulent plasma motions at decay times.

There is an EIS observation of the active region available prior to the start of the flare, at 00:45:02 UT. Nonthermal velocity maps at this nonflaring time (not shown in Figure 3) for the two hottest ions (Fe XXIII and Fe XXIV) are either nonexistent or “noisy,” as expected. However the cooler ion, Fe XVI, already shows nonthermal broadening in the region where the solar flare occurs. During this preflare time, over the ranges of $-891''86 \leq x \leq -814''06$ and $134''48 \leq y \leq 206''48$, the space-averaged nonthermal velocity ($\langle v_{\text{nth}} \rangle$) for Fe XVI is 17.82 ± 9.81 km s^{-1} .

⁵ 94 Å is chosen since it suffers from less saturation compared to 131 Å.

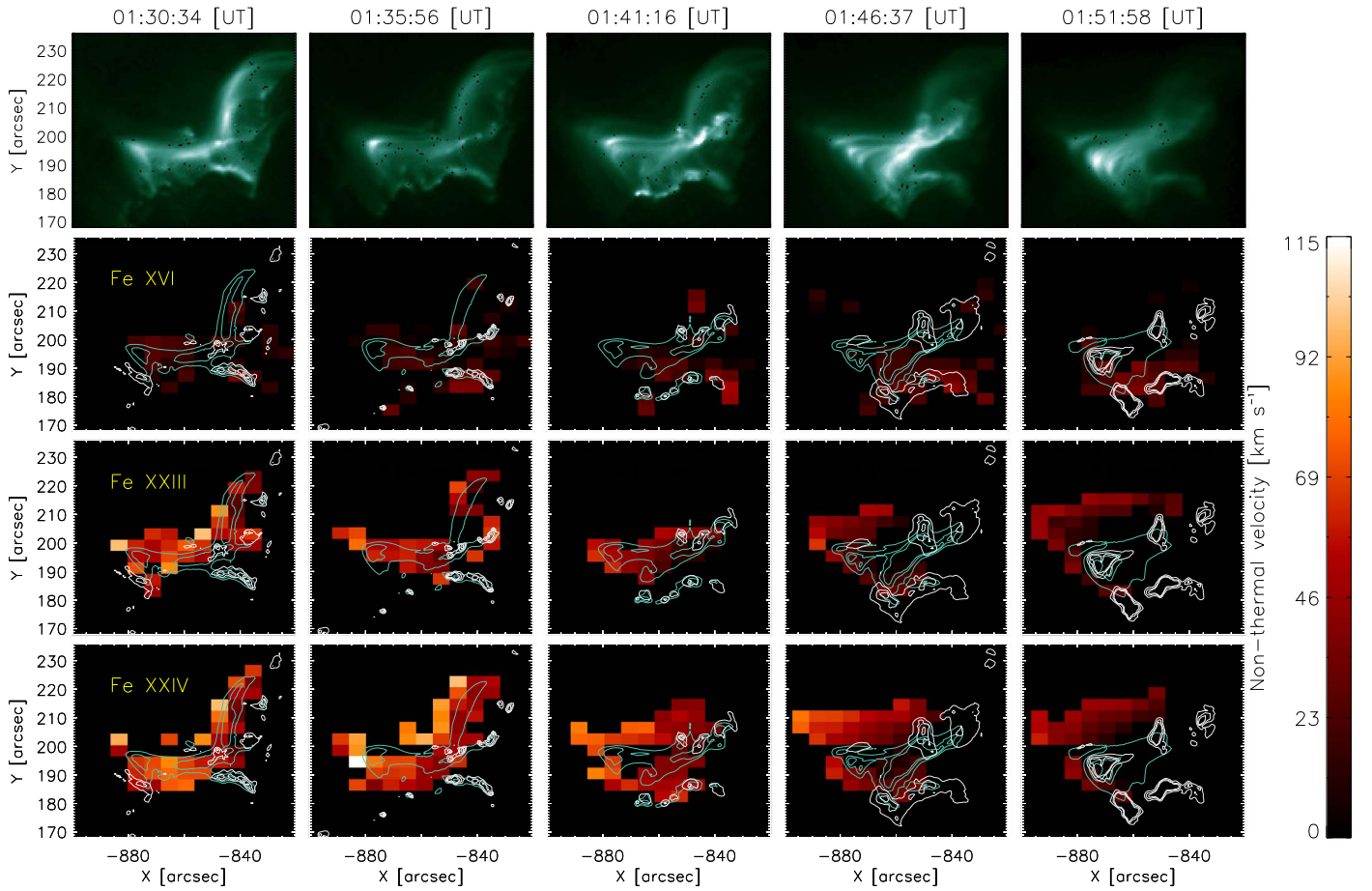


Figure 3. AIA 94 Å images (row 1) and nonthermal velocity maps (rows 2–4) for solar flare SOL2013-05-15T01:45 at five observation times. Rows 2–4 each study a different ion: Fe XVI, Fe XXIII, and Fe XXIV. AIA data are overlaid, blue contour lines show the AIA channel 94 Å intensity levels that range between 25% and 80% (of the maximum 94 Å image value) highlighting the coronal source and certain loop tops, and white contours show the 304 Å intensity levels that range between 20% and 90% (of the maximum 304 Å image value) highlighting the flare ribbons.

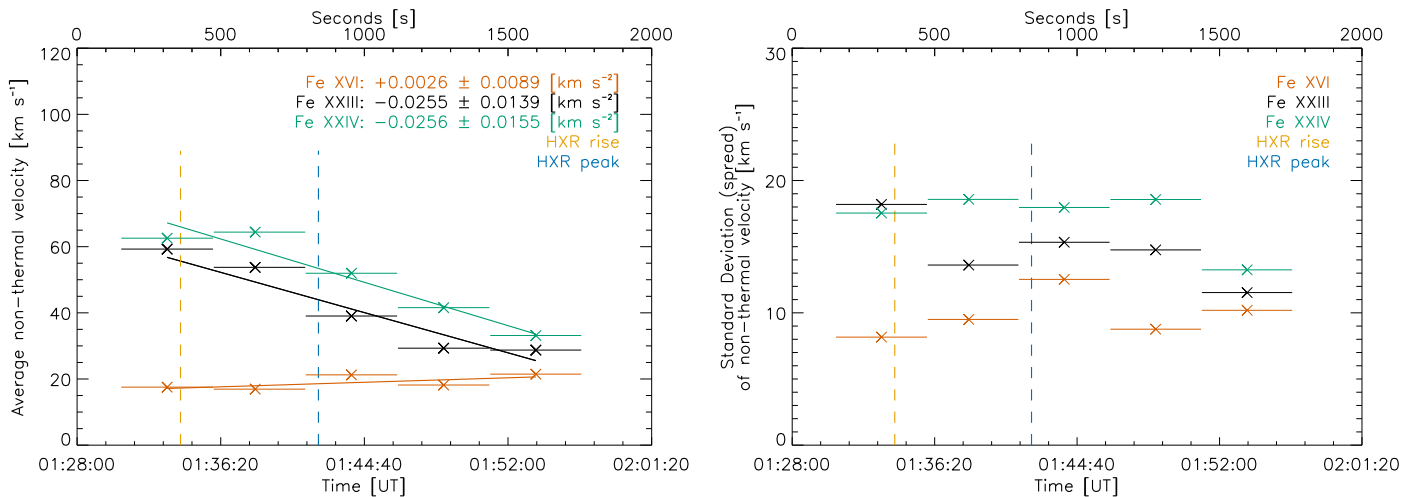


Figure 4. Space-averaged nonthermal velocity $\langle v_{nth} \rangle$ (left) and standard deviation (spread) of the nonthermal velocity values (right) calculated from all pixels shown in each map in Figure 3, versus time for Fe XVI (orange), Fe XXIII (black), and Fe XXIV (teal). The data points are positioned in the center of the raster time. The approximate times of the HXR rise and peak are shown by the yellow and blue dashed lines in each panel. The values of $d\langle v_{nth} \rangle / dt \pm$ uncertainty (km s^{-2}) are stated in the legend (left panel).

For the flare times, Figure 4 (left) shows the space-averaged nonthermal velocity calculated from all the values displayed in each map in Figure 3. The space-averaged nonthermal velocity $\langle v_{nth} \rangle$ versus time for Fe XVI, Fe XXIII, and Fe XXIV is shown

in orange, black, and teal respectively. A linear fit is used to determine the rate at which $\langle v_{nth} \rangle$ changes for each ion ($d\langle v_{nth} \rangle / dt$), the value of which is stated in the Figure 4 legend. Horizontal bars in Figure 4 show the raster time of the

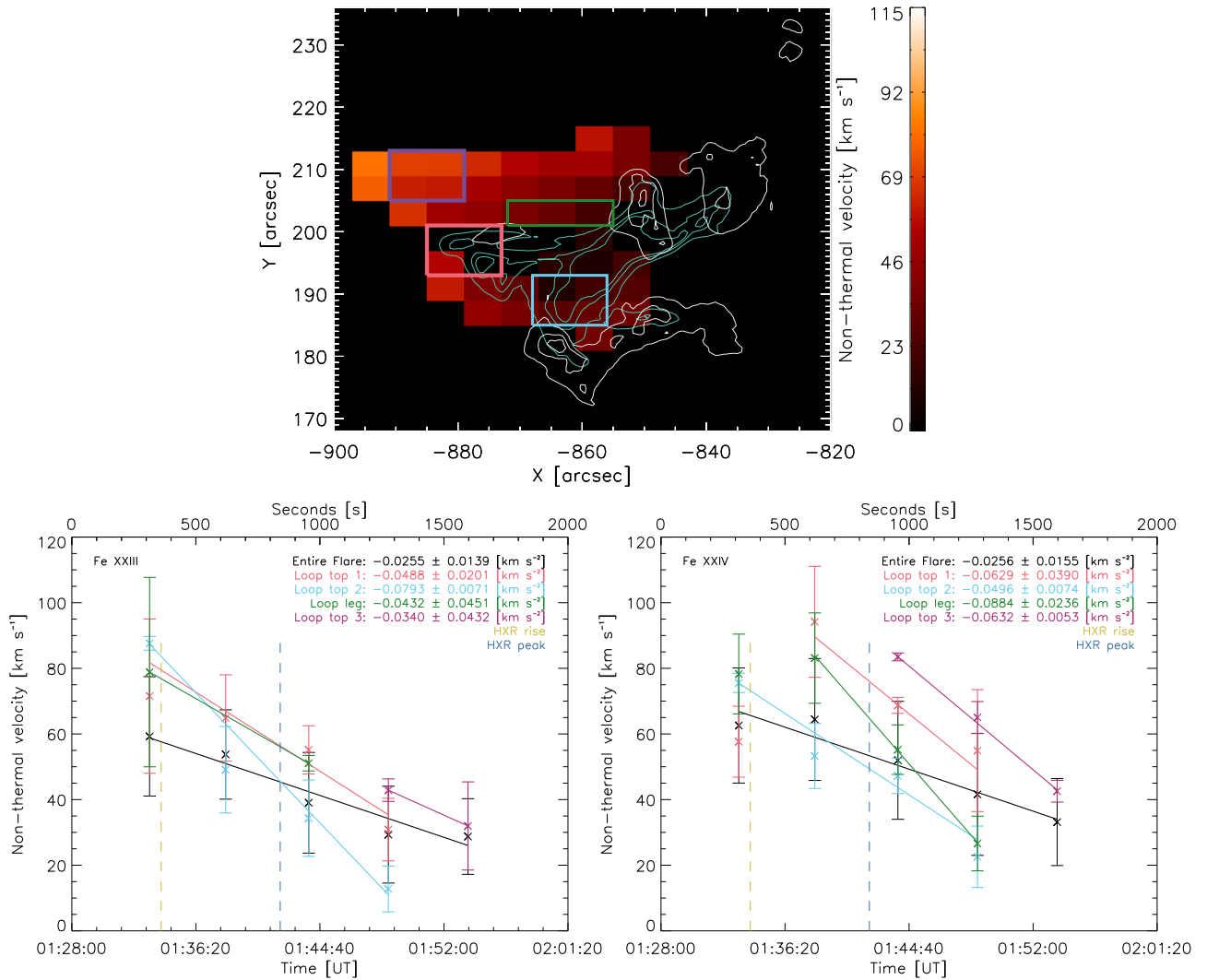


Figure 5. Top: Fe XXIV nonthermal velocity map at time 01:46:37 UT with the chosen extracted regions highlighted by the pink, purple, blue, and green boxes. Pink and blue boxes cover coronal loop tops (named “loop top 1” and “loop top 2” respectively), the green box covers part of the loop leg connected to “loop top 1,” and the purple box covers a region where bright pixels appear at later times (after the HXR peak and named “loop top 3”). Contours from AIA channel 94 Å with intensity levels that range between 25% and 80% of the maximum 94 Å image value (blue) and channel 304 Å with intensity levels ranging between 20% and 90% of the maximum 304 Å image value (white) are also plotted. Bottom: nonthermal velocity against time for Fe XXIII (left) and Fe XXIV (right) for each extracted region (pink, blue, green, and purple) and for all pixels (space-averaged $\langle v_{\text{nth}} \rangle$) in the Figure 3 map (black). The gradient \pm uncertainty ($d\langle v_{\text{nth}} \rangle / dt$ in km s^{-2}) of each fit are shown in the legend. The approximate rise and peak times of HXR emission are shown by the yellow and dark blue dashed lines in each panel, respectively. Raster time bars have been omitted from this figure for clarity; the data points are positioned in the center of the raster time.

observation with the data points located in the center. The standard deviation (spread) of all v_{nth} values in each map is also shown in Figure 4 (right). Overall, the standard deviation (spread of v_{nth} values) in each map remains fairly constant for each ion as the flare progresses (over the rise, peak, and decay) remaining at approximately 10 km s^{-1} , 15 km s^{-1} , and 18 km s^{-1} for Fe XVI, Fe XXIII, and Fe XXIV respectively. However at the last observation time, all ions have similar standard deviation values. The standard deviation (spread) values are used to calculate the uncertainties for $d\langle v_{\text{nth}} \rangle / dt$.

In general, and as expected, the hotter ions, Fe XXIII and Fe XXIV, have greater values of space-averaged nonthermal velocity $\langle v_{\text{nth}} \rangle$ compared to the cooler ion, Fe XVI. The space-averaged nonthermal velocity of the hotter ions Fe XXIII and Fe XXIV peaks at the beginning of the flare ($\langle v_{\text{nth}} \rangle \approx 60\text{--}65 \text{ km s}^{-1}$) and then decreases as the flare evolves, decreasing at a similar rate for both ions (to values between $\langle v_{\text{nth}} \rangle \approx 30\text{--}35 \text{ km s}^{-1}$),

with a deceleration of $d\langle v_{\text{nth}} \rangle / dt = -0.0255 \pm 0.0139 \text{ km s}^{-2}$ and $d\langle v_{\text{nth}} \rangle / dt = -0.0256 \pm 0.0155 \text{ km s}^{-2}$ respectively.

Unlike the hotter ions, $d\langle v_{\text{nth}} \rangle / dt$ for Fe XVI remains fairly constant. Furthermore, as previously mentioned, prior to the flare at 00:45:02 UT, Fe XVI shows a space-averaged nonthermal velocity of $\langle v_{\text{nth}} \rangle = 17.82 \pm 9.81 \text{ km s}^{-1}$, which is almost identical to the value of $\langle v_{\text{nth}} \rangle$ at the onset of the flare of $\langle v_{\text{nth}} \rangle = 17.53 \pm 8.16 \text{ km s}^{-1}$. Thus, the overall space-averaged nonthermal velocity for Fe XVI does not change significantly during the flare.

3.2. Extracted Map Regions: Temporal Changes in v_{nth}

Using the nonthermal velocity maps in Figure 3, Figure 5 identifies several key features of the flare for further study (e.g., loop tops, loop leg) and shows how the Fe XXIII and Fe XXIV nonthermal velocities within these regions evolve in time, while Figure 6 examines how the nonthermal velocity for

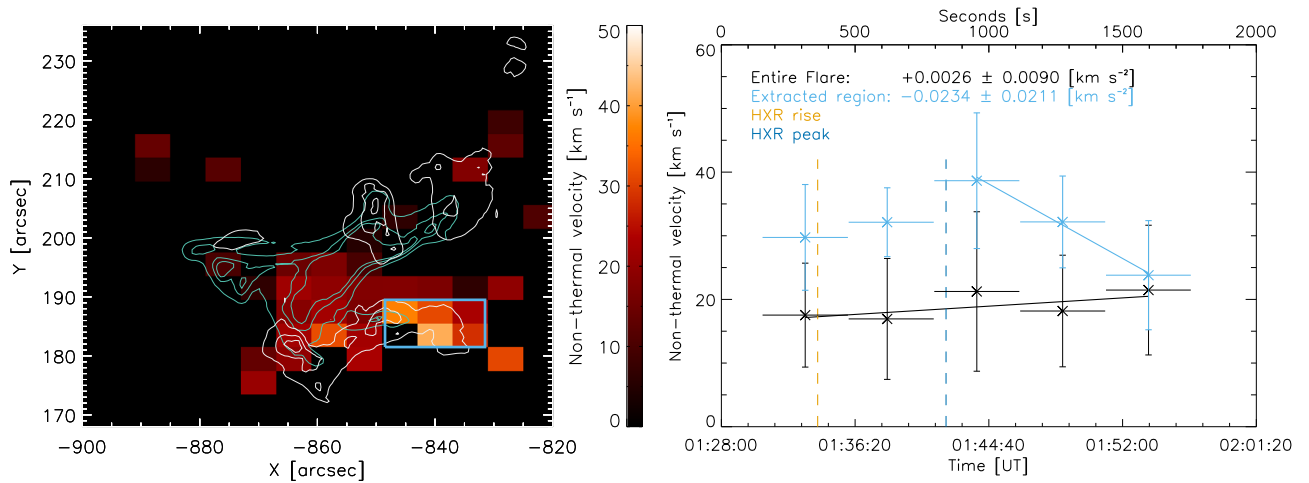


Figure 6. Nonthermal velocity map (left) of Fe XVI at time 01:46:37 UT with AIA 304 Å contours ranging between 20% and 90% of the maximum 304 Å image value (white) and 94 Å contours ranging between 25% and 80% of the maximum 94 Å image value (blue). The blue box shows the area extracted. Fe XVI nonthermal velocity against time (right) for the extracted region (blue) and for all pixels (space-averaged $\langle v_{\text{nth}} \rangle$) in the Figure 3 map (black). The gradient \pm uncertainty (dv_{nth}/dt (km s^{-2})) of each linear fit are shown in the legend. The approximate rise and peak times of HXR emission are shown by the yellow and dark blue dashed line respectively.

Fe XVI evolves with time in one region close to the southern flare ribbon. In each extracted region, the average nonthermal velocity (denoted simply as v_{nth} to distinguish it from the space-averaged value of the entire map $\langle v_{\text{nth}} \rangle$) is calculated plus the standard deviation (spread of v_{nth} values in each region). For data points where only one pixel was available the uncertainty was determined using the uncertainty given for $\Delta\lambda$ by the Gaussian fit. Overall the nonthermal velocity within all of the chosen regions in Figure 5 decreases as the flare evolves. We note that some data are missing in Figure 5, due to missing pixels at certain times.

3.2.1. Coronal Loop Top Regions

In Figure 3 (top row), the AIA 94 Å data show multiple loops in the flare. First, to study the nonthermal velocity in the different coronal loop tops in more detail, the pixels covering two identified loop top regions were extracted, highlighted by the pink and blue boxes in Figure 5. Here, “loop top 1” will refer to the pink box, which contains the loop top of the larger loop situated at the greater radial distance, and “loop top 2” will refer to the blue box containing the loop top of the smaller loop located at the smaller radial distance.

For both Fe XXIII and Fe XXIV, pixels are available for study in both regions “loop top 1” and “loop top 2” at all times except 01:51:58 UT. For Fe XXIV, at all times apart from the first studied (01:30:34 UT), the nonthermal velocity of “loop top 1” (pink) is greater than “loop top 2” (blue). We see a similar trend for Fe XXIII. For both ions and at all times, neglecting 01:30:34 UT, the nonthermal velocity in “loop top 1” is either greater than or approximately equal (at 01:46:37 UT) to the space-averaged nonthermal velocity of the entire map ($\langle v_{\text{nth}} \rangle$). For “loop top 2,” the values of nonthermal velocity are greater at early times but quickly fall below the values of $\langle v_{\text{nth}} \rangle$ seen in Figure 4.

In each region, we investigate how the nonthermal velocity changes with time using linear fitting and by calculating the gradient dv_{nth}/dt . In “loop top 1” and “loop top 2” for both Fe XXIII and Fe XXIV, the decline in the nonthermal velocity (dv_{nth}/dt) occurs at a faster rate than the decline in the space-averaged nonthermal velocity across the entire map

($d\langle v_{\text{nth}} \rangle/dt$). Overall, the analysis shows that dv_{nth}/dt varies in different regions across the maps, which might suggest: (1) the energy of the plasma motions is drained more efficiently in certain regions (e.g., for heating and/or particle acceleration) and/or (2) the mechanism producing the macroscopic motions diminishes quicker in certain regions.

In Figure 5, we also choose a region covering “loop top 3” (purple box). This covers the flare loops at the greatest radial distance, mainly produced at later times in the flare, after the peak in HXR. Located above both “loop top 1” and “loop top 2,” this region is not observed in the AIA 94 Å contours ranging between 25% and 80% of the maximum 94 Å image value. For the data points available, the nonthermal velocity in “loop top 3” also decreases as the flare progresses. Comparing each loop top region shows that at a given time (when available), the largest values of v_{nth} occur at the greater radial distance so that v_{nth} (“loop top 3”) $>$ v_{nth} (“loop top 1”) $>$ v_{nth} (“loop top 2”).

3.2.2. Loop Leg

In Figure 5, part of the loop leg that appears to be connected to “loop top 1” is highlighted by the green box (this will be referred to as the “loop leg”). As with “loop top 1,” the Fe XXIV nonthermal velocity in “loop leg” only decreases with time after 01:35:56 UT, once the HXR emission begins to rise. Hence, for Fe XXIV we only consider observation times from 01:35:56 UT, where v_{nth} decreases with time when studying the gradient (dv_{nth}/dt) in this region. For Fe XXIV, from 01:35:56 UT onward, “loop leg” v_{nth} values are smaller than “loop top 1” v_{nth} values and they decrease quicker over the same time period compared to “loop top 1” (with gradient $dv_{\text{nth}}/dt = -0.0884 \pm 0.0236 \text{ km s}^{-1}$ compared to $dv_{\text{nth}}/dt = -0.0629 \pm 0.0390 \text{ km s}^{-1}$, respectively). For Fe XXIII, only times of 01:30:34 UT and 01:41:16 UT are available for study. For Fe XXIII, the values of “loop leg” v_{nth} are similar to “loop top 1” values and v_{nth} decreases at approximately the same rate in both regions (with gradient $dv_{\text{nth}}/dt = -0.0432 \pm 0.0451 \text{ km s}^{-1}$ compared to $dv_{\text{nth}}/dt = -0.0488 \pm 0.0201 \text{ km s}^{-1}$, respectively).

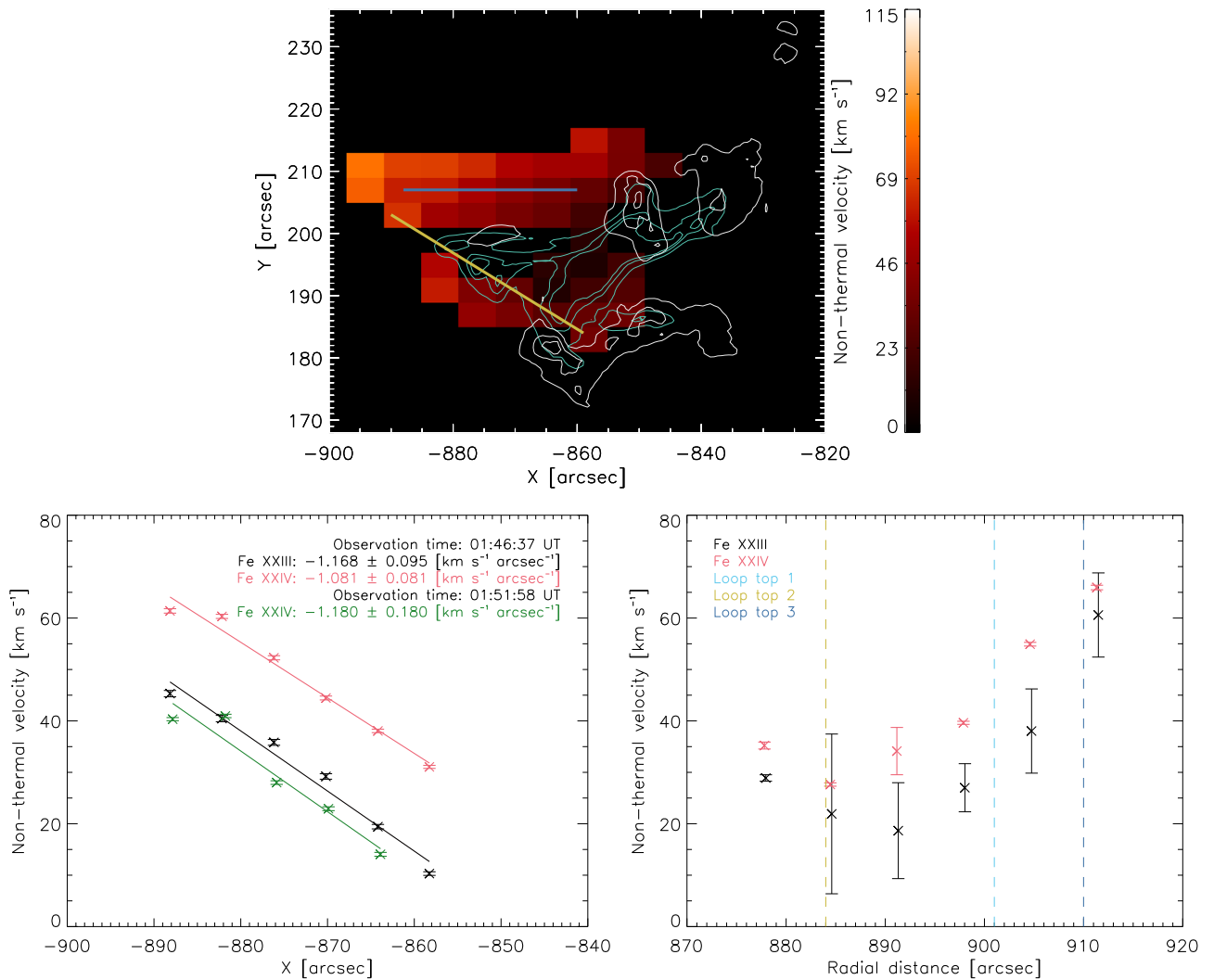


Figure 7. Nonthermal velocity map (top) of Fe XXIV at 01:46:37 UT. Changes in nonthermal velocity with space are examined along the line joining the coronal loop top source, loop leg, and northern ribbon (blue line) and along the line connecting the upper and lower loop top sources (yellow line). Bottom left: nonthermal velocity versus solar x (along the blue line) for Fe XXIII and Fe XXIV at 01:46:37 UT (black and pink respectively) and for Fe XXIV at 01:51:58 UT (green). The gradient \pm uncertainty (dv_{nth}/dx ($\text{km s}^{-1} \text{arcsec}^{-1}$)) of each linear fit are shown in the legend. Bottom right: nonthermal velocity versus radial distance $r = \sqrt{x^2 + y^2}$ (along the yellow line) for Fe XXIII and Fe XXIV at 01:46:37 UT (black and pink respectively). The light blue, yellow, and dark blue dashed lines show the approximate location of “loop top 1,” “loop top 2,” and “loop top 3,” respectively.

3.2.3. Southern Ribbon

We also study how the nonthermal velocity from the cooler ion Fe XVI changes with time in one region, shown by the blue box in Figure 6, where the Fe XVI nonthermal velocity appears to increase along the lower edge of the flare. The AIA 304 Å data show that this area corresponds to the southern flare ribbon on the map (although the exact height of the Fe XVI emission is unknown). Extracting the average v_{nth} in this region and comparing it to the space-averaged value of the entire flare ($\langle v_{\text{nth}} \rangle$) shows that v_{nth} in this area is higher than $\langle v_{\text{nth}} \rangle$ at each studied time. For example, at 01:35:56 UT $\langle v_{\text{nth}} \rangle = 16.93 \pm 9.50 \text{ km s}^{-1}$ but $v_{\text{nth}} = 32.13 \pm 5.41 \text{ km s}^{-1}$ in the extracted blue box region.

Initially, the nonthermal velocity of the extracted region increases, coinciding with the rise in HXR which begins at 01:34:00 UT (indicated by the yellow dashed line in Figure 6). The nonthermal velocity peaks at 01:41:16 UT with a value of $v_{\text{nth}} = 38.65 \pm 10.66 \text{ km s}^{-1}$ and at approximately the same time as the peak in HXR at 01:42:00 UT, as shown by the blue

dashed line in Figure 6. After the peak in HXR, the nonthermal velocity of the extracted region begins to decrease. By the last observation time, at 01:51:58 UT, the value of the nonthermal velocity v_{nth} is approximately the same value as the space-averaged nonthermal velocity of the entire flare ($\langle v_{\text{nth}} \rangle$).

3.3. Spatial changes in v_{nth}

In the maps of nonthermal velocity in Figure 3, v_{nth} changes in space with spatial patterns becoming clearer during and after the peak in HXR, particularly for the hotter ions Fe XXIII and Fe XXIV. Here we focus on the observation at 01:46:37 UT, where spatial patterns in v_{nth} are clearly seen for both Fe XXIII and Fe XXIV (although similar patterns can be observed during the time close to the peak in HXR at 01:41:16 UT and at the later time of 01:51:58 UT). We consider changes in space along the two lines shown in Figure 7: the horizontal blue line covers the region from a loop apex (previously “loop top 3”) and along the upper loop leg; the diagonal yellow line passes through the middle of the flare coronal source and multiple

coronal loop tops. There are no Fe XVI pixels close to “loop top 3,” thus only the hotter ions are considered in Figure 7. It was difficult to study spatial changes at earlier times during the rise in HXRs. This was due to the compactness of the loop tops and the more chaotic pattern of nonthermal velocity at these times, suggesting that the spatial distribution of turbulence may be more random and possibly dependent on fluctuations in local conditions at early times in the flare.

For each line, we plot the nonthermal velocity against position (v_{nth} against x for the blue line and against radial distance $r = \sqrt{x^2 + y^2}$ for the diagonal yellow line), and calculate the gradient dv_{nth}/dx from the values determined along the blue line. Along the blue line, we also consider changes in nonthermal velocity versus x at the later time of 01:51:58 UT for Fe XXIV, shown in green in Figure 7. Due to insufficient pixels, Fe XXIII was not included on the plot at this time. Along the blue line, only single pixels from Figure 3 are considered.

Along the blue line at time 01:46:37 UT, for both Fe XXIII and Fe XXIV, the values of v_{nth} fall as we move from the loop apex along the loop leg. The nonthermal velocity decreases at a similar rate for both Fe XXIII and Fe XXIV with $dv_{\text{nth}}/dx = -1.168 \pm 0.095 \text{ km s}^{-1} \text{ arcsec}^{-1}$ and $dv_{\text{nth}}/dx = -1.081 \pm 0.081 \text{ km s}^{-1} \text{ arcsec}^{-1}$, respectively. Along the blue line at 01:51:58 UT, the values of nonthermal velocity for Fe XXIV are approximately $\approx 20\text{--}25 \text{ km s}^{-1}$ lower than at the previous time but the values decrease along x at roughly the same rate of $dv_{\text{nth}}/dx = -1.180 \pm 0.180 \text{ km s}^{-1} \text{ arcsec}^{-1}$. Along the blue line at 01:51:58 UT, the values of nonthermal velocity for Fe XXIV are similar to those for Fe XXIII at 01:46:37 UT.

As discussed, the AIA 94 Å maps (top row in Figure 3) show multiple flare loops (studied using “loop top 1,” “loop top 2,” and “loop top 3” in Figure 5). The diagonal yellow line in Figure 7 cuts through these different loop tops. To determine the nonthermal velocity along this line, the average of 2 pixels covering the line is used. The approximate locations of “loop top 1,” “loop top 2,” and “loop top 3” are highlighted in Figure 7 (bottom right) by the light blue, yellow, and dark blue dashed lines respectively. For both Fe XXIII and Fe XXIV, the nonthermal velocity decreases overall from the larger loops at the greater radial distance to smaller loops at a smaller radial distance. For Fe XXIV, from “loop top 3” to “loop top 1” the nonthermal velocity decreases at a faster rate than from “loop top 1” to “loop top 2”. At the radial distances smaller than “loop top 2” the nonthermal velocity increases for both ions.

It is interesting to note that the fall in nonthermal velocity (turbulence) is approximately linear along the blue line connecting the loop apex and loop leg at times corresponding to the peak in HXRs and after (and approximately linear along the yellow radial line connecting the different loop tops). In recent modeling studying the effects of an extended spatial distribution of turbulence on electron acceleration, e.g., Stackhouse & Kontar (2018), the turbulent acceleration diffusion coefficient is modeled as a decreasing exponential in space (along the coronal loop) since the form of the spatial distribution of turbulence accelerating electrons in the flare is usually unknown. However, although the exact relationship between the diffusion coefficient and the macroscopic velocity v_{nth} is not entirely clear, we can see that the decrease in v_{nth} in space along the loop is much slower than exponential, suggesting that the turbulence may influence the acceleration

or transport of electrons over a larger spatial extent than modeled to date. Such observations are extremely useful for constraining future simulations studying the link between spatially distributed turbulence and electron acceleration and transport in flares.

3.4. Turbulent Kinetic Energy Density Maps

In Kontar et al. (2017), a space-averaged value of nonthermal velocity $\langle v_{\text{nth}} \rangle$ in the flaring corona of SOL2013-05-15T01:45 is converted to a space-averaged coronal kinetic energy $\langle K \rangle$ [erg] using

$$\langle K \rangle = \frac{3}{2} \cdot 1.3m_p \langle v_{\text{nth}} \rangle^2 n_p V \quad (4)$$

where m_p is the proton mass (g) (and $1.3m_p$ is the mean ion mass for solar coronal abundances; Reames 2014), n_p is proton number density (cm^{-3}) (taken as a single space-averaged coronal value at each time in Kontar et al. 2017), and V is the plasma volume (cm^3).

For the first time, in order to calculate the kinetic energy K at every spatial pixel shown in the nonthermal velocity maps (Figure 3), we employ spectral line density diagnostics, specifically using the Fe XIV (264.7889 Å/274.2037 Å) intensity ratio (Young 2011). This method provides the electron number density n_e in regions of the plasma where Fe XIV is produced at ≈ 2 MK. Making the assumption that $n_e = n_p$, n_p can then be determined at every spatial pixel across the flare at each observation time, as shown in the top panel of Figure 8. The obvious issue with density determination using this Fe XIV intensity ratio is that it might not provide a true indication of the density within the hotter flaring coronal loops where Fe XIV is not present, particularly during the rise and peak of the flare. However, we stress it is the only suitable density diagnostic available for the flare observation. We also note that Fe XIV (274.2037 Å) contains a cool blend at 274.1804 Å formed at ≈ 0.63 MK. Density maps were also created accounting for this blend using the automatic EIS fitting software and we did not see any noticeable differences in the density maps produced when this blend was accounted for in the fitting procedure.

The density maps (row 1 of Figure 8) show that initially there is an increase in plasma density where the flare is located, shown by the AIA 94 Å contours, compared to the surrounding solar atmosphere. As the flare progresses, the area around the flare increases in density until almost the entire field of view of the map has a higher density than the background density observed in the first map. As with the density surrounding the flare, the density of the area covering the AIA 94 Å contours increases as the flare evolves. At 01:51:58 UT the area of highest density corresponds to a region where no values of nonthermal velocity are observed for Fe XXIII and Fe XXIV.

The turbulent kinetic energy density (K/V (erg cm^{-3})) was determined for each ion at each observation time, shown in rows 2, 4, and 6 of Figure 8 for Fe XVI, Fe XXIII, and Fe XXIV respectively using the spatially resolved Fe XIV density maps and the nonthermal velocity maps shown in Figure 3. For clarity, the maps in Figure 8 show $\log_{10}(K/V)$. For each ion studied in Figure 8, we also show the kinetic energy density (K/V) maps using the single space-averaged values of coronal number density calculated from RHESSI X-ray spectroscopy and taken from Kontar et al. (2017; rows 3, 5, and 7). Using a single space-averaged value of coronal number density from

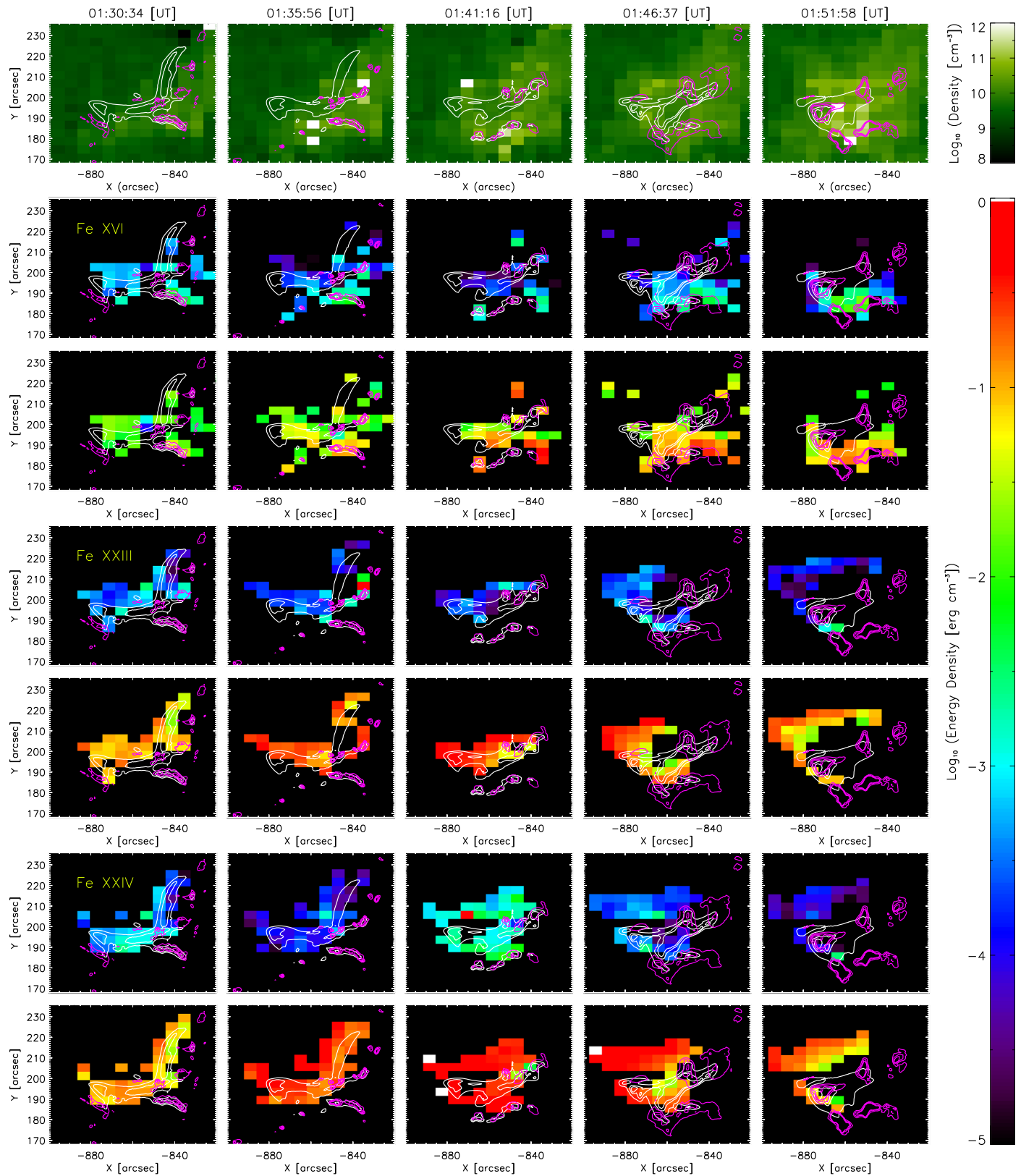


Figure 8. Density ($n_e \text{ cm}^{-3}$) and kinetic energy density ($K/V \text{ erg cm}^{-3}$) maps of the flare (time increasing from left to right) overlaid with AIA 94 Å contours (ranging between 35% and 70% of the maximum 94 Å value; white) and 304 Å contours (ranging between 20% and 90% of the maximum 304 Å value; pink). Top row: (\log_{10}) density maps for each observation time created using the Fe XIV 264.79 Å/274.20 Å intensity ratio. The second and third rows show the (\log_{10}) kinetic energy density maps for Fe XVI using the spatially varying EIS density ratio (row 2) and single value space-averaged coronal density determined from X-ray observations in Kontar et al. (2017; row 3). Rows 4 and 5 show the same results (as row 2 and 3) but for Fe XXIII, while rows 6 and 7 show the same results but for Fe XXIV. For $\log_{10}(K/V)$, the background level (no values of v_{nth} or K/V) is set to a value 10^{-5} for plotting purposes only.

X-ray spectroscopy should provide an approximate upper limit on both the number and kinetic energy density in each region of the flare. Using the space-averaged coronal density produces a map of kinetic energy density that only depends on the variations in nonthermal velocity and, hence, similar patterns emerge spatially in these (K/V) maps and the nonthermal velocity maps in Figure 3. Interestingly, when the spatial changes in density are taken into account, the patterns observed in the nonthermal velocity maps (particularly where higher values of nonthermal velocity are seen at greater radial heights in Section 3.3) are diminished (compared to the constant single density case), particularly along the coronal loop apex radial line. Moreover, it was determined in Jeffrey et al. (2015) that the coronal loop top source of the flare can contain strong gradients in both temperature and number density along the radial direction opposite to the guiding magnetic field, varying by an order of magnitude with the density decreasing, and temperature increasing, toward greater radial heights.

Taking into account changes in density alongside changes in v_{nth} allows us to see important local inhomogeneities in the spatial distribution of the kinetic energy available. Moreover, even with the presence of local fluctuations, the results are highly suggestive that an almost identical reservoir of kinetic energy from turbulent plasma motions is available in large parts of the flaring corona at a given time, indicating that this energy could be extracted by particles in the form of acceleration and heating in multiple parts of the flare. Away from the coronal loop top, we also see higher values of the kinetic energy density in cooler regions denoted by the Fe XVI emission. In regions closer to the flare ribbons, where the Fe XVI nonthermal velocity was shown to increase before the peak in HXR emission, the larger number densities produce large values of kinetic energy density in the region. However, the efficiency of particle acceleration will depend on the local plasma conditions and whether acceleration can overcome Coulomb collisions (local density), possibly leading to increased heating instead in very dense regions.

4. Summary of the Observations

The nonthermal broadening of spectral lines is a key sign of macroscopic plasma motions leading to turbulence in flares. In this paper, we mapped the nonthermal broadening (velocity) across a large region in a solar flare at different times and found the following main observations.

1. As is often observed, but not discussed, the presence of nonthermal broadening in flares is not a localized phenomenon. The maps in Figure 3 show the presence of nonthermal velocities (turbulence) across the entire flare region covering the loop apex, loop legs, and close to ribbon features lower in the atmosphere.⁶
2. Indeed as shown by, e.g., Antonucci & Dodero (1995) and Doschek et al. (2014), nonthermal broadening (turbulence) is greatest for the hottest ions, Fe XXIII and Fe XXIV, and in general reduces with ion temperature, again suggesting that there is a temperature gradient to turbulence in plasma. Further, the MHD modeling of Gordovskyy et al. (2016) suggests that higher nonthermal velocities (turbulence) lead to greater heating and/or

acceleration (particle energization) and hence higher ion temperatures, since more energy is dissipated.

3. Turbulence is not localized but the hottest ions available for study, Fe XXIII and Fe XXIV, show that the nonthermal broadening is often greatest in regions that coincide to the loop tops of magnetic loops, where it is expected (in a standard model) that the primary energy release and the bulk of electron energization occur.
4. Considering the two hottest ions, Fe XXIII and Fe XXIV, Figure 4 shows that turbulence is greatest at the start of the flare and reduces over time as the mechanism producing turbulence dies away as expected. Before the peak in HXR, the maps display a more random distribution of nonthermal velocities across the flare, but during and after the peak we see a clear spatial pattern with the largest nonthermal velocities occurring in the loop apex and decreasing toward the positions of the flare ribbons. The spatial variation in nonthermal velocity from a loop apex along the loop leg (and along the radial line connecting the different loop tops) appears to reduce at approximately a linear rate.
5. At the beginning of the flare, the nonthermal velocity in the coronal source is higher than the average nonthermal velocity across the entire flare. Turbulence (nonthermal velocity) then reduces in this region at a faster rate than the flare overall, until the nonthermal velocity in the coronal region is similar to the value of the average nonthermal velocity in the entire flare. This might suggest that energy from turbulence in the coronal source is dissipated at a higher rate than in the rest of the flare. Alternatively, the mechanism producing turbulence may die faster in this region. In turbulence theory, the energy deposition rate indeed increases with v_{nth} since energy per mass unit/time $\sim v_{\text{nth}}^3/L_{\perp}$ where L_{\perp} is the perpendicular scale of turbulence (e.g., Goldreich & Sridhar 1995). In general, we find different values of dv_{nth}/dt in different regions of the corona.
6. Turbulence is present in cooler, lower heights in the flare, i.e., among the flare ribbons. This is suggested by the increase and peak in nonthermal velocity in the extracted region of Fe XVI in Figure 6, which coincides with the rise and peak in HXR as the flare progresses. After the peak in HXR, the region continues to have an increased amount of turbulence which decreases until it reaches a similar level to the average value of Fe XVI nonthermal velocity in the entire flare. We note that the EIS time resolution cannot determine if turbulence appears before or affects the energetic electrons in the region or if the turbulence is generated by the energetic electrons reaching the lower atmosphere.
7. When converted to a turbulent kinetic energy density, the use of a more realistic spatially varying number density shows that, although the nonthermal velocities decrease as we move away from the loop apex, changing densities away from the apex diminish the variations (or at least large gradients) in kinetic energy at different points in the flare, suggesting that similar levels of kinetic energy may be available in regions away from the loop apex and into coronal loop legs and the lower corona (although the efficiency of particle energization in denser regions may be reduced).

⁶ Although the nonthermal broadening is aligned with features here, the exact height of turbulence in the atmosphere is not known from this data.

This detailed study suggests that turbulence plays a role throughout the flaring corona and has a complex inhomogeneous spatial and temporal structure and evolution, not considered in previous studies. We await the availability of hot density diagnostics for plasma >10 MK from future instrumentation which will greatly improve the determination of the kinetic energy (density) in flaring coronal loops, helping to uncover both interesting local fluctuations and constrain the availability of kinetic energy in the flaring corona. This work should be of interest to the modeling community and, in particular, help to constrain both the mechanism of turbulence in flares and its spatial and temporal distributions which are of great importance to the production and form of accelerated electrons in flares.

N.L.S.J. gratefully acknowledges the current financial support from the Science and Technology Facilities Council (STFC) Grant ST/V000764/1 and previous support from STFC Grant ST/P000533/1. M.S. gratefully acknowledges the financial support from the Northumbria University RDF studentship. The authors acknowledge IDL support provided by STFC. The work is supported by an international team grant [Solar flare acceleration signatures and their connection to solar energetic particles](#) from the International Space Sciences Institute (ISSI) Bern, Switzerland. Hinode is a Japanese mission developed and launched by ISAS/JAXA, with NAOJ as domestic partner and NASA and UKSA as international partners. It is operated by these agencies in cooperation with ESA and NSC (Norway). CHIANTI is a collaborative project involving George Mason University, the University of Michigan (USA), University of Cambridge (UK) and NASA Goddard Space Flight Center (USA).

Data Availability

For the data analysis, we used Interactive Data Language (IDL) and SolarSoftWare (SSW). Hinode/EIS data are available at the Hinode Science Data Centre Europe <http://sdc.uio.no/sdc/>. SDO/AIA data are available at <http://jsoc.stanford.edu/>.

ORCID iDs

Morgan Stores  <https://orcid.org/0000-0002-6060-8048>
 Natasha L. S. Jeffrey  <https://orcid.org/0000-0001-6583-1989>
 Eduard P. Kontar  <https://orcid.org/0000-0002-8078-0902>

References

Allred, J. C., Kowalski, A. F., & Carlsson, M. 2015, *ApJ*, 809, 104
 Antonucci, E., & Doderio, M. A. 1995, *ApJ*, 438, 480

Antonucci, E., Gabriel, A. H., Acton, L. W., et al. 1982, *SoPh*, 78, 107
 Aschwanden, M. J., Caspi, A., Cohen, C. M. S., et al. 2017, *ApJ*, 836, 17
 Brooks, D. H., & Warren, H. P. 2016, *ApJ*, 820, 63
 Carlsson, M., & Stein, R. F. 1992, *ApJL*, 397, L59
 Culhane, J. L., Harra, L. K., James, A. M., et al. 2007, *SoPh*, 243, 19
 De Pontieu, B., Title, A. M., Lemen, J. R., et al. 2014, *SoPh*, 289, 2733
 Del Zanna, G., & Mason, H. E. 2018, *LRSF*, 15, 5
 Dere, K. P., Del Zanna, G., Young, P. R., Landi, E., & Sutherland, R. S. 2019, *ApJS*, 241, 22
 Dere, K. P., Landi, E., Mason, H. E., Monsignori Fossi, B. C., & Young, P. R. 1997, *A&AS*, 125, 149
 Doschek, G. A., Feldman, U., Kreplin, R. W., & Cohen, L. 1980, *ApJ*, 239, 725
 Doschek, G. A., McKenzie, D. E., & Warren, H. P. 2014, *ApJ*, 788, 26
 Emslie, A. G., Dennis, B. R., Shih, A. Y., et al. 2012, *ApJ*, 759, 71
 Goldreich, P., & Sridhar, S. 1995, *ApJ*, 438, 763
 Gordovskyy, M., Kontar, E. P., & Browning, P. K. 2016, *A&A*, 589, A104
 Graham, D. R., Hannah, I. G., Fletcher, L., & Milligan, R. O. 2013, *ApJ*, 767, 83
 Jeffrey, N. L. S., Fletcher, L., & Labrosse, N. 2016, *A&A*, 590, A99
 Jeffrey, N. L. S., Fletcher, L., & Labrosse, N. 2017, *ApJ*, 836, 35
 Jeffrey, N. L. S., Fletcher, L., Labrosse, N., & Simões, P. J. A. 2018, *SciA*, 4, 2794
 Jeffrey, N. L. S., Kontar, E. P., & Dennis, B. R. 2015, *A&A*, 584, A89
 Kahler, S. W., & Kreplin, R. W. 1991, *SoPh*, 133, 371
 Klein, K.-L., & Dalla, S. 2017, *SSRv*, 212, 1107
 Kontar, E. P., Bian, N. H., Emslie, A. G., & Vilmer, N. 2014, *ApJ*, 780, 176
 Kontar, E. P., Perez, J. E., Harra, L. K., et al. 2017, *PhRvL*, 118, 155101
 Kosugi, T., Matsuzaki, K., Sakao, T., et al. 2007, *SoPh*, 243, 3
 Krucker, S., Battaglia, M., Cargill, P. J., et al. 2008, *A&ARv*, 16, 155
 Larosa, T. N., & Moore, R. L. 1993, *ApJ*, 418, 912
 Lemen, J. R., Title, A. M., Akin, D. J., et al. 2012, *SoPh*, 275, 17
 Levens, P. J. 2018, PhD thesis, Univ. of Glasgow
 Lin, R. P., Dennis, B. R., Hurford, G. J., et al. 2002, *SoPh*, 210, 3
 Melrose, D. B. 1994, *ApJS*, 90, 623
 Miller, J. A., Cargill, P. J., Emslie, A. G., et al. 1997, *JGR*, 102, 14631
 Milligan, R. O. 2011, *ApJ*, 740, 70
 Milligan, R. O. 2015, *SoPh*, 290, 3399
 Musset, S., Kontar, E. P., & Vilmer, N. 2018, *A&A*, 610, A6
 Parker, E. N. 1957, *JGR*, 62, 509
 Petrosian, V. 2012, *SSRv*, 173, 535
 Polito, V., Dudík, J., Kašparová, J., et al. 2018, *ApJ*, 864, 63
 Polito, V., Testa, P., & De Pontieu, B. 2019, *ApJL*, 879, L17
 Priest, E. 2014, *Magnetohydrodynamics of the Sun* (Cambridge: Cambridge Univ. Press)
 Priest, E., & Forbes, T. 2000, *Magnetic Reconnection* (Cambridge: Cambridge Univ. Press)
 Reames, D. V. 2014, *SoPh*, 289, 977
 Stackhouse, D. J., & Kontar, E. P. 2018, *A&A*, 612, A64
 Sweet, P. A. 1958, in *Electromagnetic Phenomena*, ed. B. Lehnert, Vol. 6 (Cambridge: Cambridge Univ. Press), 123
 Warmuth, A., & Mann, G. 2016, *A&A*, 588, A116
 Warren, H. P., Brooks, D. H., Ugarte-Urra, I., et al. 2018, *ApJ*, 854, 122
 Young, P. 2011, *Deriving Densities, Column Depths and Filling Factors from Hinode/EIS Data*, Technical Report, EIS Software Note, https://sohftp.nascom.nasa.gov/solarsoft/hinode/eis/doc/eis_notes/15_DENSITY/eis_swnote_15.pdf